

## Entangled chain dynamics of polymer knots in extensional flow

Demosthenes Kivotides, S. Louise Wilkin, and Theo G. Theofanous

*Department of Chemical Engineering, Center for Risk Studies and Safety, University of California, Santa Barbara, California 93117, USA*

(Received 29 June 2009; published 29 October 2009)

We formulate a coarse-grained molecular-dynamics model of polymer chains in solution that includes hydrodynamic interactions, thermal fluctuations, nonlinear elasticity, and topology-preserving solvent mediated excluded volume interactions. The latter involve a combination of potential forces with explicit geometric detection and tracking of chain entanglements. By solving this model with numerical and computational methods, we study the physics of polymer knots in a strong extensional flow (Deborah number  $De=1.6$ ). We show that knots slow down the stretching of individual polymers by obstructing via entanglements the “natural,” unraveling, and flow-induced chain motions. Moreover, the steady-state polymer length and polymer-induced stress values are smaller in knotted chains than in topologically trivial chains. We indicate the molecular processes via which the rate of knot tightening affects the rheology of the solution.

DOI: [10.1103/PhysRevE.80.041808](https://doi.org/10.1103/PhysRevE.80.041808)

PACS number(s): 61.25.he, 47.57.Ng, 47.50.-d

### I. INTRODUCTION

Topological chain motion constraints (entanglements) are a determining factor in polymer dynamics in both equilibrium and nonequilibrium situations. Indeed [1–4], entanglements in melts and dense solutions under strain determine the rate of buildup of elastic stresses and, assuming a constant homogeneous strain rate field, their values at steady state. In this context, numerous works [3] based on the confining tube idea of Doi and Edwards [2], in conjunction with the reptation model of de Gennes [5] have been developed in order to take into account entanglement effects on the rheology of melts and solutions. The underlying physical processes correspond to complex many-body statistical physics problems that are not satisfactorily understood. On the other side, intrachain entanglements can be important even in single macromolecule physics since they are responsible for the permanence of knotted polymer configurations. Indeed, knots in polymers are not rare [6–11] since, indicatively, the probability of self-knotting in self-avoiding walks on cubic lattices increases as  $1-e^{-cn}$ , where  $c$  is a constant and  $n$  is the number of monomers. Knots are central mathematical objects. Since the pioneering studies of Thomson [12], they are strongly associated with vortex dynamics and similar topological defects in classical [13], statistical [14], and quantum [15] field theories. However, polymer dynamics is very different from vortex dynamics. Among other reasons, this is due to the phenomenon of vortex reconnection that has no counterpart in polymers. Vortex reconnection acts as a dynamical topology factor, i.e., it alters the topology of vorticity during the evolution of the system [14,16,17]. There is no analogous mechanism in polymers; thus, excluding chain scission phenomena in strong flows [18], a polymer knot can unravel only by migrating toward either of the chain ends.

Knotted biomolecules in solution in the cell are characterized by functional problems in the context of replication, transcription, and recombination processes as discussed in Ref. [19]. In this context, it is important to develop methods for the detection of knots and for the characterization of the geometry and topology of macromolecules [20]. Employing

such methods, Taylor [21] detected trefoil and figure-of-eight knots in proteins. We approach knotted polymers from a different perspective. We assume that a chain is knotted (thus, the topology is given), and we concentrate on physics. The physics of open knotted polymers is a topic of intensive research. They have been studied in equilibrium or nonequilibrium, as well as in many- or single-chain contexts. In the single knotted chain context, Quake [22] and Lai [23] analyzed departures of knotted polymers in solution from the Rouse model behavior typical of linear chains indicating a long-time relaxation mode not predicted by the latter [22]. Employing molecular-dynamics methods, Kim and Klein [24] studied a similar problem by placing a trefoil knot in a melt of linear chains in equilibrium and measuring the unknotting time scale. This study has been extended to nonequilibrium situations by Saitta and Klein [25] who, after placing a trefoil knot within a system of 35 linear chains, stretched the sample. They showed that the knot nucleates a stretching-induced crystallization. Our contribution differs from these studies in that we are mainly interested in strongly nonequilibrium situations, and our main emphasis is on rheological (rather than phase transitional) implications of stretched polymer knots. Equally important, we concentrate on polymer solutions rather than melts, and we focus on system behavior at time scales much larger than those allowed by practical Hamiltonian molecular-dynamics computations (3 ns in Ref. [25]). The physics of polymer knots in nonequilibrium has attracted a lot of interest [26–30]. In the relevant works, the knotted chain ends were arrested by optical tweezers [26,27], or parallel walls [28], and then pulled apart. Topics of interest were the speed with which a knot diffuses toward either of the chain ends or the scaling of the knot size (i.e., the number of monomers participating in the knot) with time. Another work by Saitta *et al.* [31] employed Car-Parrinello (*ab initio*) molecular dynamics and focused on polymer scission under similar stretching mechanisms.

In this paper, we tackle different questions. We analyze the effects of knotted polymers on solution rheology by placing them in an extensional flow field with a homogeneous steady strain rate. In this case, the flow field exerts drag forces on every part of a knotted chain, rather than on the

two ends only, and these forces depend on the chain configuration. Knot effects on solution rheology are quantified via the direct computation of macromolecular contribution to the solution stress, which is the most important rheological quantity. Most importantly, previously employed methods in the study of knots did not enforce chain uncrossability constraints; thus, phantom chain events were typical [27]. For example, following a phantom chain event, Vologodskii [27] stopped the calculation and restarted it from a time prior to the phantom chain event with a different random number sequence in the computation of Brownian force. In contrast, we explicitly enforce and dynamically resolve chain uncrossability constraints by significantly extending and integrating in our model analogous methodologies [32,33].

Next, we offer an exposition of a coarse-grained molecular-dynamics (CGMD) model of polymer chains in solution that includes hydrodynamic interactions, thermal fluctuations, nonlinear elasticity, and topology-preserving solvent mediated excluded volume interactions. In a nutshell, the model combines a solution theoretic Brownian dynamics analysis, a feature shared with Ref. [27], with uncrossability constraint enforcement methods, following the approach previously applied to melts by Padding and Briels (PB) [32] but developing it further, since the original method was found unable to preserve knot topologies. Moreover, we have developed our own approach in gauging the various dynamical factors in the governing equations. For all these reasons, and since entangled chain computations of the type presented here are far from standard, we pay emphasis to the completeness of exposition, providing full mathematical details for the model. Subsequently, we describe the numerical methods employed in the solution of the proposed model, and we provide details about the algorithmic structure of the computational code. Finally, we present results indicating the impact of figure-of-eight and granny polymer knots on extensional solution rheology.

## II. MODEL

At the most fundamental (within classical physics) level, polymer solutions are modeled as Hamiltonian systems describing solvent and polymer molecular motion [34]. Regarding the polymers, one can coarse grain their dynamics by averaging the equations of motion over lengths comparable to chain contour length and times comparable to chain relaxation times. Due to their collective nature, the spectra of the resulting coarse-grained polymer dynamics involve relatively slow frequencies and wavelengths so that, during resolvable chain motion transients, the lighter solvent molecules are in local equilibrium (Brownian limit) and obey hydrodynamic laws. In this way, coarse-grained polymers are similar to Brownian lines or, more precisely, taking into account Brownian-motion-induced entropic elasticity effects and excluded volume interactions, they can be described as interacting, uncrossable, and Brownian elastic strings [35].

### A. Fluid dynamics of entangled polymer solutions

An isothermal incompressible polymeric fluid  $\mathcal{F} = \{\mathbf{u}(\mathbf{x}, t), \mathbf{r}^c(\xi, t)\}$ ,  $c = 1, \dots, N_c$  is specified by the solution

velocity field  $\mathbf{u}(\mathbf{x}, t)$  and the contours  $\mathbf{r}^c(\xi, t)$  of  $N_c$  polymer chains. Here,  $\mathbf{x}$  denotes a point in space,  $\xi$  is the arclength parametrization along the chains, and  $t$  is the time. By employing appropriate initial and boundary conditions (and assuming the existence of solutions), we evolve the fluid according to coupled nonlinear laws. In particular, at macroscopic scales, the solution dynamics become the dynamics of a viscoelastic fluid whose stress has contributions from both solvent and polymer molecules [36],

$$\rho \frac{\partial \mathbf{u}}{\partial t} + \rho \mathbf{u} \cdot \nabla \mathbf{u} = -\nabla p + \nabla \cdot \boldsymbol{\sigma}, \quad (1)$$

$$\nabla \cdot \mathbf{u} = 0, \quad (2)$$

where  $\rho$  is the solution mass density,  $\mathbf{u}$  is the solution-velocity field,  $p$  is the pressure field, and  $\boldsymbol{\sigma}$  is the solution stress tensor

$$\boldsymbol{\sigma} = \boldsymbol{\sigma}^p + \eta_s(\boldsymbol{\kappa} + \boldsymbol{\kappa}^T). \quad (3)$$

The first term on the right-hand side is the polymer contribution, while the second one is the solvent contribution according to Newton's law with  $\eta_s$  being the solvent viscosity and  $\boldsymbol{\kappa} = (\nabla \mathbf{u})^T$  being the transpose solution-velocity gradient tensor. Stress  $\boldsymbol{\sigma}^p$  is a functional of polymer chain configuration taking into account contributions from chain kinetic energy, elasticity, and excluded volume interactions and, in the present model, is computed via CGMD of the polymer chains. In order to simplify the problem and avoid solving Eqs. (1) and (2) self-consistently with CGMD, we prescribe the solution flow field kinematically, and we consider only uniaxial extensional flow

$$\mathbf{u} = \boldsymbol{\kappa} \cdot \mathbf{r}, \quad (4)$$

$$\boldsymbol{\kappa} = \begin{pmatrix} \dot{\epsilon} & 0 & 0 \\ 0 & -\dot{\epsilon}/2 & 0 \\ 0 & 0 & -\dot{\epsilon}/2 \end{pmatrix}, \quad (5)$$

where  $\dot{\epsilon}$  is the rate of strain in units of  $\text{s}^{-1}$ . Consequently, our analysis is applicable only to simple homogeneous strain rate flows, where either the solution is very dilute and the polymers have small effects on solvent motion, or other external forces (like, for example, surface tension in filament-thinning rheometers [37,38]) that counterbalance the growth of elastic stresses as the strain increases.

Extending previous works on polymer melts and solutions [32,33,39–43], we describe the polymers via entangled chain dynamics (ECD). Notably, the ECD model formulated here differs from the effective tube theoretic ECD that has been developed for dense solutions and melts (for example, Refs. [44–46]). The present model can resolve chain motions at space-time scales smaller than the tube size  $a$  and characteristic, tube theoretic, and entanglement strand time  $\tau_e$  and can be used to assess the validity of the hypotheses of more macroscopic ECD models.

Each chain contour  $\mathbf{r}^c$  is discretized into  $N_{b,c}$  massive beads (linked Lagrangian markers) that are connected by  $N_{s,c} = N_{b,c} - 1$  massless springs. In this way, the bead mass represents the mass of the chain segment corresponding to a

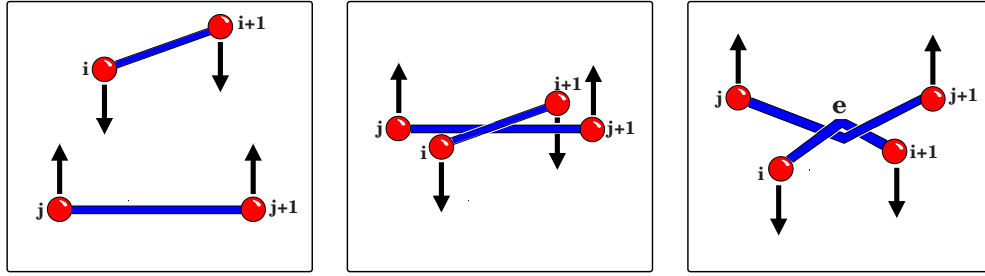


FIG. 1. (Color online) The formation of entanglement  $e$  upon collision of spring  $i$  with spring  $j$ . The arrows indicate bead direction of motion. Notice the zigzag spring contour induced by the entanglement.

spring. We signify beads by  $b$  and springs by  $s$ . The total number of beads is  $N_b = \sum_{c=1}^{N_c} N_{b,c}$ , and the total number of springs is  $N_s = \sum_{c=1}^{N_c} N_{s,c}$ . As shown in Figs. 1 and 2, springs (in general) are not straight segments between beads, but zigzag lines punctuated by entanglement positions. Notably, following Padding and Briels [32], springs are assumed to be slippery elastic strings, so all subsegments of a particular spring possess the same elastic tension. We signify entanglements by index  $e$ . The total number of entanglements is  $N_e(t) = \sum_{c=1}^{N_c} \sum_{s=1}^{N_{s,c}} N_{e,s}^c(s, t)$ , where  $N_{e,s}^c(s, t)$  is the number of entanglements of spring  $s$  in chain  $c$  at time  $t$ . Beads and entanglements are collectively called objects and denoted by index  $o$ . Segments between any two objects are called connectors and denoted by index  $q$ . The total number of connectors is  $N_q(t) = \sum_{c=1}^{N_c} \sum_{s=1}^{N_{s,c}} N_{q,s}^c(s, t)$ , where  $N_{q,s}^c(s, t)$  is the number of connectors of spring  $s$  in chain  $c$  at time  $t$ . The basic dynamical objects in our model are vectors of dimension  $3(N_b + N_e)$  in direct correspondence with the object (bead and entanglement) coordinates  $i$  [ $i = 1, \dots, 3(N_b + N_e)$ ]. In the mathematical statement of the problem, it is necessary to introduce a number of auxiliary functions describing the correspondence between beads, entanglements, springs, connectors, and object coordinates since all of these entities intermingle in the governing equations. In particular, we define two forms of the integer valued function  $b$ , i.e.,  $b = b(i)$  that for each bead coordinate  $i$  returns bead  $b$ , and  $b = b(s)$  that for each spring  $s$  returns bead  $b$  at the spring's origin. Similarly, we define two forms of the integer valued function  $o$ , i.e.,  $o = o(i)$  that for each object coordinate  $i$  returns object  $o$ , and  $o = o(q)$  that for each connector  $q$  returns object  $o$  at the connector's origin. We also define an integer function  $s = s(i)$  that for each bead coordinate  $i$  returns the index of the spring between beads  $b(i)$  and  $b(i) + 1$ , and an integer func-

tion  $q = q(i)$  that for each object coordinate  $i$  returns the index of the connector between objects  $o(i)$  and  $o(i) + 1$ . Two other useful functions are  $q = q^c(s)$ , where  $s = 1, \dots, N_{s,c}$ , which for every spring  $s$  of chain  $c$  returns connector  $q$  at the spring origin, and  $s = s^c(q)$  that for every connector  $q$  of chain  $c$  returns spring  $s$  ( $s = 1, \dots, N_{s,c}$ ) to which the connector belongs. Finally, the integer function  $d = d(i)$  returns, for each object coordinate  $i$ , the corresponding Cartesian direction index ( $d = 1, \dots, 3$ ).

The governing stochastic differential equation for the bead coordinates is [33,47]

$$m_b \frac{d^2 r_i}{dt^2} \equiv m_b \frac{dv_i}{dt} = {}^e F_i + {}^h F_i + {}^t F_i + {}^{ev} F_i. \quad (6)$$

Here,  $i$  runs over the bead coordinates,  $m_b$  is the bead mass,  $r_i \equiv r_{d(i)}^{b(i)}$  is the component of the position  $\mathbf{r}^b$  of bead  $b(i)$  along the direction  $d(i)$ , and, similarly,  $v_i \equiv v_{d(i)}^{b(i)}$  is the component of the velocity  $\mathbf{v}^b$  of bead  $b(i)$  along the direction  $d(i)$ . The force  ${}^h F_i \equiv {}^h F_{d(i)}^{b(i)}$  is the component of the hydrodynamic force  ${}^h \mathbf{F}^b$  on bead  $b(i)$  along the direction  $d(i)$ . The elastic force  ${}^e F_i$  is equal to the difference of the elastic forces of the connectors that are attached to  $b(i)$ , i.e.,  ${}^e F_i = {}^e F_{d(i)}^{q(i)} - {}^e F_{d(i)}^{q(i)-1}$ , where  ${}^e F_{d(i)}^{q(i)}$  is the component along  $d(i)$  of the elastic force  ${}^e \mathbf{F}^q$  of connector  $q(i)$  that extends between objects  $o(i)$  and  $o(i) + 1$ . The force  ${}^{ev} F_i \equiv {}^{ev} F_{d(i)}^{b(i)}$  is the solvent mediated excluded volume interaction  ${}^{ev} \mathbf{F}^b$  on bead  $b(i)$  along the direction  $d(i)$ . Finally,  ${}^t F_i$  is the force causing thermal bead fluctuations.

Spring  $s$  corresponds to the spring vector  $\mathbf{Q}^s = \mathbf{r}^{b(s)+1} - \mathbf{r}^{b(s)}$ ; and, similarly, if  $\mathbf{r}^o$  is the position of object  $o$ , connector  $q$  corresponds to the connector vector  $\mathbf{Q}^q = \mathbf{r}^{o(q)+1} - \mathbf{r}^{o(q)}$ . Notably (Fig. 2),  $\mathbf{Q}^s$  corresponds to the actual chain segment between the corresponding beads only in case where the spring does not carry any entanglements. The polymer contribution to the solution stress  $\boldsymbol{\sigma}^p$  is given by a modified Kramers formula

$$\begin{aligned} \boldsymbol{\sigma}^p = & \nu \sum_{s=1}^{N_{s,c}} \left\langle \frac{q^c(s) + N_{q,s}^c(s) - 1}{\sum_{q=q^c(s)} Q^q \cdot {}^e \mathbf{F}^q} \right\rangle - \nu \sum_{b=1}^{N_{b,c}} \sum_{s=1}^{N_{s,c}} B_{bs} \langle \mathbf{Q}^s \cdot {}^{ev} \mathbf{F}^b \rangle \\ & - \nu m_b \sum_{b=1}^{N_{b,c}} \langle (\mathbf{v}^b - \mathbf{u}^b)(\mathbf{v}^b - \mathbf{u}^b) \rangle, \end{aligned} \quad (7)$$

where  $\nu = N_{A,c} / M$  is the number of polymers per unit solution volume,  $c$  is the polymer mass concentration, i.e., the total

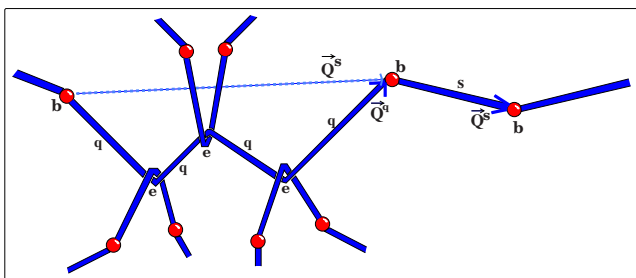


FIG. 2. (Color online) Explanation of various symbols employed in the governing equations.

mass of the dissolved chains divided by the solution volume,  $M$  is the molecular mass in Da,  $N_A$  is Avogadro's number,  $\mathbf{u}^b$  is the solution velocity at the position of bead  $b$ , and  $B_{bs}$  are defined as [36]

$$B_{bs} = \frac{s}{N_b}, \quad s < b, \quad (8)$$

$$B_{bs} = - \left[ 1 - \frac{s}{N_b} \right], \quad s \geq b, \quad (9)$$

and the angular brackets denote ensemble averages over many entangled chains. The first term of the right-hand side denotes the dominant contribution of chain elasticity, the second term denotes the contribution of excluded volume interactions, and the third is the contribution of the kinetic energy of the chains. Before we proceed, we need to define the various terms on the right-hand side of the Langevin equation (6).

### B. Elastic forces

We model the elastic force  ${}^e\mathbf{F}^q$  of connector  $q$  with the finitely extensible nonlinear elastic law (FENE) [39]

$${}^e\mathbf{F}^q = \frac{H\ell^s}{1 - (\ell^s/\ell_0)^2} \hat{\mathbf{Q}}^q, \quad (10)$$

where  $H=3k_B T/[N_{K,s}(\beta b_K)^2]$  is the elastic constant,  $N_{K,s}$  is the number of Kuhn lengths per spring,  $b_K$  is Kuhn's length,  $\ell_0=N_{K,s}b_K$  is the maximum spring length,  $\hat{\mathbf{Q}}^q=\mathbf{Q}^q/(\sqrt{\mathbf{Q}^q \cdot \mathbf{Q}^q})$  is the unit vector along the direction of connector  $q$ ,  $\ell^s$  is the length of spring  $s=s^c(q)$  to which connector  $q$  belongs, and the resting length of each spring is zero. Noting that all subsegments of a particular spring possess the same elastic tension, the latter takes into account the zigzag spring outline [32]

$$\begin{aligned} \ell^s &= \sum_{q=q^c(s)}^{q^c(s)+N_{q,s}^c(s)-1} \sqrt{\mathbf{Q}^q \cdot \mathbf{Q}^q} \\ &= \sum_{q=q^c(s)}^{q^c(s)+N_{q,s}^c(s)-1} \sqrt{(\mathbf{r}^{\sigma(q)+1} - \mathbf{r}^{\sigma(q)}) \cdot (\mathbf{r}^{\sigma(q)+1} - \mathbf{r}^{\sigma(q)})}. \end{aligned} \quad (11)$$

Note that, when  $\beta=1$ ,  $H$  becomes the elastic constant for an ideal chain after employing the Gaussian approximation of the probability density function for the end to end distance in the computation of the free energy. This elastic law choice is motivated by a number of considerations:

(a) The strain rates in the computations correspond to chain Deborah numbers  $\text{De}_1=\tau_1\dot{\epsilon}$  (where  $\tau_1$  is the longest chain relaxation time) larger than unity. At these strain rates (and for sufficiently long times) the chains are expected to stretch to a length comparable to their maximum length. Thus, the linear elasticity Gaussian spring law is not appropriate. Since all our results refer to good solvents and include hydrodynamic interaction effects, an appropriate estimate of  $\tau_1$  is the Zimm longest relaxation time [39,40]

$$\tau_1^Z = \frac{\eta_s b_K^3}{k_B T} \left( \frac{v_{ev}}{b_K^3} \right)^{6\nu-3} N_{K,c}^{3\nu}, \quad (12)$$

where  $N_{K,c}$  is the number of Kuhn lengths per chain,  $\nu=0.588$  takes into account excluded volume effects (according to renormalization-group analysis refinements of Flory mean-field theory) that cause chain swelling in a good solvent,  $v_{ev}$  is the experimental excluded volume, and  $v_{ev}/b_K^3$  quantifies the quality of the solvent becoming unity in the athermal solvent case.

(b) Our working macromolecule is adequately modeled by a freely jointed chain, and Eq. (10) is Warner's approximation [48] to the inverse Langevin function that captures elasticity effects in such polymers. Wavelengths smaller than Kuhn's length are not excited, and there are no small-scale bending mode effects even close to the maximum polymer extension. Consistently, the springs are resistant to stretching but not to bending. More general models of elastic strings with explicit bending elasticity are discussed in Refs. [49,50]. Notably, Eq. (10) assumes that the internal spring dynamics reaches a thermodynamic steady state at time scales much faster than the applied strain rate; thus, in our computations, the spring Deborah number  $\text{De}_0=\tau_0\dot{\epsilon}$  (where  $\tau_0$  is the spring relaxation time) is much smaller than unity. The time  $\tau_0$  is computed from Eq. (12) by replacing  $N_{K,c}$  with  $N_{K,s}$ . Notably, this requirement allows a rational choice of  $N_{s,c}$ , the number of springs per chain. This number must be sufficiently large (so that, correspondingly,  $N_{K,s}$  is sufficiently small) for the condition  $\text{De}_0 \ll 1$  to hold. Moreover, since  $N_{s,c}$  fixes  $\ell_0$ ,  $\beta$  is the only free parameter that gauges elastic effects in the definition of  ${}^e\mathbf{F}^q$ .

(c) Our chain model contains excluded volume interactions and our computations involve good solvents; thus, the ideal chain assumption used in the derivation of the FENE law is not applicable. The purpose of the empirical constant  $\beta$  [51–53] is to rectify (in an *ad hoc* fashion) this discrepancy by introducing, in the calculation of  $H$ , an effective Kuhn's length  $b'_K=\beta b_K$ .

### C. Viscous drag and thermal fluctuation forces

We neglect the effects of macroscopic velocity gradients on the force exerted by the flow on the particle, as well as short-range lubrication interactions in the computation of resistance tensors [47]. Subsequently, the hydrodynamic force becomes [47,54,55]

$${}^h\mathbf{F}_i = - \sum_{j=1}^{3N_b} \zeta_{ij} (\mathbf{v}_j - \mathbf{u}_j), \quad (13)$$

where  $\zeta_{ij}$  is the hydrodynamic friction tensor, while  $\mathbf{u}_j \equiv \mathbf{u}_{d(j)}^{b(j)}$  is the component of the (macroscopic) solution velocity  $\mathbf{u}^b$  at position  $\mathbf{r}^{b(j)}$  along  $d(j)$ . Denoting by  $\boldsymbol{\mu}=\boldsymbol{\zeta}^{-1}$  the mobility tensor,  $\mathbf{v}_j - \mathbf{u}_j = -\sum_{i=1}^{3N_b} \boldsymbol{\mu}_{ji} {}^h\mathbf{F}_i$  is the Stokes flow induced by  $N_b$  point forces  ${}^h\mathbf{F}^b$  at the bead positions. We only consider unbounded fluid domains, and we employ an approximate solution of the corresponding Stokes flow problem that has the property of preserving, when employed in the computation of the symmetric diffusion tensor  $D_{ij}$ , the

positive-definite character of the latter even when the beads are too close together

$$\sum_{j=1}^{3N_b} \zeta_{ij} D_{jl} = \sum_{j=1}^{3N_b} D_{ij} \zeta_{jl} = k_B T \delta_{il}, \quad (14)$$

where  $k_B$  is the Boltzmann constant,  $T$  is the temperature of the solvent, and  $\delta_{il}$  is the Kronecker delta. Equivalently,  $\boldsymbol{\mu} = \mathbf{D}/(k_B T)$ . We employ the Rotne-Prager-Yamakawa (RPY) [56] diffusion tensor

$$D_{ij} = \frac{k_B T}{6\pi\eta_s a} \delta_{ij}, \quad b(i) = b(j), \quad (15)$$

$$D_{ij} = \frac{k_B T}{8\pi\eta_s R_{ij}} \left[ \left( 1 + \frac{2a^2}{3R_{ij}^2} \right) \mathbf{I} + \left( 1 - \frac{2a^2}{R_{ij}^2} \right) \frac{\mathbf{R}_{ij} \mathbf{R}_{ij}}{R_{ij}^2} \right],$$

$$R_{ij} \geq 2a, b(i) \neq b(j), \quad (16)$$

$$D_{ij} = \frac{k_B T}{6\pi\eta_s a} \left[ \left( 1 - \frac{9R_{ij}}{32a} \right) \mathbf{I} + \frac{3R_{ij} \mathbf{R}_{ij} \mathbf{R}_{ij}}{32a R_{ij}^2} \right],$$

$$R_{ij} < 2a, b(i) \neq b(j), \quad (17)$$

where  $a$  denotes the effective bead radius,  $\mathbf{I}$  is the unit  $3 \times 3$  tensor,  $\mathbf{R}_{ij} = \mathbf{r}^{b(j)} - \mathbf{r}^{b(i)}$ , and  $R_{ij} = \sqrt{\mathbf{R}_{ij} \cdot \mathbf{R}_{ij}}$ . The thermal fluctuation force  ${}^t F_i$  is [47]

$${}^t F_i = \sum_{j=1}^{3N_b} a_{ij} f_j, \quad (18)$$

where  $a_{ij}$  are related to  $\zeta_{ij}$  by the relation

$$\zeta_{ij} = \frac{1}{k_B T} \sum_{l=1}^{3N_b} a_{il} a_{jl}, \quad (19)$$

and  $f_j$  are described by a Gaussian distribution with mean and covariance

$$\langle f_i \rangle = 0, \quad (20)$$

$$\langle f_i(t) f_j(t') \rangle = 2 \delta_{ij} \delta(t - t'), \quad (21)$$

where  $\delta(t - t')$  is the delta function.

Notably, since the mean drag force and its fluctuations are related by the generalized fluctuation dissipation relation (19), the effective bead radius gauges both of their strengths. Next, we discuss the choice of  $a$ . In a good solvent, the Flory mean-field theory and its renormalization-group refinements provide an appropriate estimate of the chain size  $R_c$  [39]

$$R_c = b_K \left( \frac{\nu_{ev}}{b_K^3} \right)^{2\nu-1} N_{K,c}^\nu, \quad (22)$$

where  $\nu = 0.588$  ( $\nu = 0.5$  in a theta solvent). By substituting  $N_{K,s}$  in place of  $N_{K,c}$  we obtain the spring size  $R_s$ . Notably, this formula is valid when  $N_{K,c}$  or  $N_{K,s}$  are larger than the number of monomers in a thermal blob, so that excluded volume effects dominate thermal effects and the chain becomes a random walk of thermal blobs. Now, we notice that,

in the Zimm theory, a chain segment corresponding to a spring diffuses as if it were a particle (a bead) with a volume proportional to the pervaded volume of the spring, i.e., due to hydrodynamic interactions, the spring moves like a solid object dragging the solvent within its pervaded volume and displacing the rest of the solvent [39]. Thus, a suitable choice of the bead radius is half of the spring size  $a \approx R_s/2$ . Defining the proportionality constant as  $2h$ , we have  $a = hR_s$ . Notably, in the case of a theta solvent,  $h$  becomes the hydrodynamic interaction parameter. Consistency requires that  $h < 0.5$  since the bead's diameter cannot be larger than the corresponding spring size. In the end,  $a = h\beta R_s$  since (in the theta solvent case)  $R_s$  is proportional to  $b_K$ , and we have introduced in the computation of  $H$  the effective Kuhn length  $b'_K = \beta b_K$ . In this way, the choice of the free parameter  $h$  fixes the strength of drag and thermal fluctuations effects.

#### D. Solvent mediated excluded volume interaction forces

Excluded volume interactions model solvent mediated long-range attractive forces between polymer chains and ensure the uncrossability of the latter. When two macromolecules collide, topology must be preserved. Since a chain is discretized into beads and the segments (springs) that join them, not only a bead can not pass through another bead, but also a spring cannot pass through another spring. In our approach, bead to bead excluded volume interactions are taken into account by potential forces that are active on scales comparable with the bead size and do not favor bead overlap. The spring to spring excluded volume interactions are contact interactions (i.e., they have infinite strength upon spring-spring contact and zero strength otherwise) and their only purpose is to ensure topology preservation. In their modeling, we have followed a more geometric approach that explicitly detects and forbids chain crossings. It is important to note that, ideally, describing a polymer chain by employing as many Lagrangian markers as Kuhn lengths and computing exactly the three-dimensional geometry of colliding dynamical lines would make any additional potential forces between beads unnecessary in the athermal solvent case. However, in our CGMD computations, the number of resolved contacts is a fraction of the actual number of contacts, and the computational entanglement dynamics are an approximation of the microscopic molecular contact dynamics; thus, the soft repulsive potential is a necessary ingredient of the model as well.

#### E. Bead-bead excluded volume interactions

We employ a soft potential model of bead to bead excluded volume interactions since it allows larger numerical time steps than the familiar Lennard-Jones potential. In particular, the potential of the excluded volume interaction at bead  $b1$  located at  $\mathbf{r}^{b1}$  generated by all other beads is

$${}^{ev} \phi^{b1} = \sum_{b2=1}^{N_b} \alpha e^{-(r^{b2} - r^{b1}) \cdot (r^{b2} - r^{b1}) / \delta^2}, \quad (23)$$

where  $\alpha$  determines the potential's strength and  $\delta$  determines the potential's range. The excluded volume force acting on bead  $b1$  is

$${}^{ev}\mathbf{F}^{b1} = -\frac{\partial {}^{ev}\phi^{b1}}{\partial \mathbf{r}^{b1}} = -\sum_{b2=1}^{N_b} \frac{2(\mathbf{r}^{b2} - \mathbf{r}^{b1})}{\delta^2} \alpha e^{-(\mathbf{r}^{b2} - \mathbf{r}^{b1}) \cdot (\mathbf{r}^{b2} - \mathbf{r}^{b1}) / \delta^2}. \quad (24)$$

In order to define  $\alpha$  and  $\delta$ , we reflect upon the physical interpretation of a bead. As mentioned above, a bead represents a chain segment of the size of a spring. Let us imagine the approach of two beads  $b1$  and  $b2$ . Their excluded volume interactions ought to prevent their overlap, i.e., they should be effective at distances on the order of the bead radius, which we have chosen to be half of the spring size. Therefore, a suitable choice of the potential range  $\delta$  could be half of the spring size,

$$\delta = R_s/2. \quad (25)$$

The excluded volume interaction energy  $\alpha$  ought to be large enough in order to prevent bead overlap; therefore, it should scale with the energy required to exclude the  $N_{K,s}$   $b1$  monomers from the total excluded volume of the  $N_{K,s}$   $b2$  monomers. Our analysis employs mean-field theoretical arguments first proposed by Flory [39,40]. Accordingly, the energy required for the exclusion of one  $b1$  monomer (that entered the  $b2$  pervaded volume) from the combined excluded volume of  $N_{K,s}$   $b2$  monomers is equal to the product of the probability  $N_{K,s} v_{ev} / R_s^3$  of finding the  $b1$  monomer within any of the  $N_{K,s}$   $b2$  monomer excluded volumes  $v_{ev}$  (that collectively comprise a fraction of the pervaded  $b2$  volume  $R_s^3$ ) with the thermal energy  $k_B T$  that must be overpowered for the exclusion to take place. Since, in principle, the  $b2$  bead should be able to exclude the whole  $b1$  chain segment at once, this number must be multiplied with  $N_{K,s}$  giving

$$\alpha = k_B T N_{K,s}^2 v_{ev} / R_s^3. \quad (26)$$

Notably, this treatment of excluded volume interactions does not involve any adjustable constants.

### F. Spring-spring excluded volume interactions

As shown in Fig. 1, two colliding chains should not be able to pass through each other. This effect is modeled via the introduction of spring-spring contact excluded volume interactions. There are two methodologies. The one followed by Larson and coworkers [33,43] is more physical in its scope and introduces strong, repulsive, and short-range potentials between springs. The advantage of this approach is that its computational implementation is relatively simple. On the other hand, hard potentials severely restrict the time steps allowed for numerical stability (thus, it is difficult to follow the evolution of the system for large periods of time), and the method does not provide a direct geometric tracking of entanglement positions. Employing a soft exponential potential [43] allows larger numerical time steps but does not guarantee chain uncrossability. For these reasons, we follow here the more geometric approach of PB who provided an excellent discussion of their method in Ref. [32], which should be consulted for an in depth exposition of their method. Upon applying the method to the dynamics of polymer knots, we found that it fails to preserve knot integrity.

Consequently, we have introduced in the PB method elements that make knot computations possible. Next, we summarize for clarity the essentials of the PB method in the context of our model, and we describe in detail our own input.

### G. Entanglements

Our analysis is an extension of the Padding and Briels approach [32] to the realm of knotted polymer dynamics. The PB method directly computes the motion of connectors in three dimensions, detecting their crossings (entanglements), and tracking the positions of the latter in time. Entanglements and disentanglements are explicitly resolved, and entanglements change the geometry of springs from straight segments connecting the end beads to zigzag lines, affecting in this way both the magnitude and the direction of elastic forces. Notably, PB assumed that entanglement dynamics occur at much faster time scales than CGMD, so that entanglements instantaneously adjust their positions to the configuration of the beads. This adjustment is realized by minimizing (with given bead positions) the total elastic energy of all springs in the system with respect to the entanglement positions. In our model, we employ FENE springs, and the corresponding spring elastic energy to be minimized is

$${}^e\Phi = \sum_{s=1}^{N_s} {}^e\phi^s = -\sum_{s=1}^{N_s} \frac{H\ell_0^2}{2} \ln|1 - (\ell^s/\ell_0)^2|. \quad (27)$$

As formula (11) for the spring length  $\ell^s$  indicates,  ${}^e\Phi$  is a function of the object (bead and entanglement) coordinates and, due to the aforesaid scale separation assumption, it is meaningful to optimize with respect to entanglement positions.

An exact test of every ECD model is provided by the computation of knotted polymer chains. This is because entanglements are expected in this case to preserve the integrity of the knot, i.e., to preserve the topology of the chain. It is important to note that our working polymer is a linear chain polymer, so the knot theory is not strictly applicable since it applies to loops [6,7,19,57]. In topology, open knots are called tangles. Tangle theory is the knot theory within a three-ball surface under the hypothesis that the ends of the polymer chain are firmly glued on the three-ball surface. This is a technical way of assuring that the polymer does not unknot by having the chain ends interfering with the knotted part. In practical computations, this is achieved by inserting the actual polymer knot far away from the chain ends. We have performed a series of calculations, where the solution is in equilibrium and the initial polymer configuration is a trefoil knot. We found that, after typically a few hundred thousand time steps, the PB method did not preserve the knot, i.e., phantom chain events (passing of two segments through each other) occurred. Accordingly, we have modified the method in three ways in order to disallow phantom chain events. Here, we shall discuss these modifications.

(a) When do two chain segments attempt to pass through each other? Padding and Briels introduced the volume

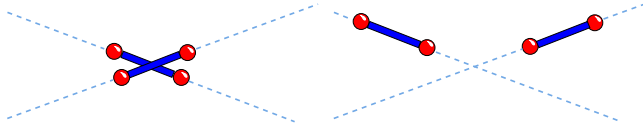


FIG. 3. (Color online) The crossing of the infinite lines corresponding to two chain segments forms an entanglement only when the crossing point belongs to both segments (left).

$$V^{ij} = (\mathbf{r}^i - \mathbf{r}^j) \cdot [(\mathbf{r}^{i+1} - \mathbf{r}^i) \times (\mathbf{r}^{j+1} - \mathbf{r}^j)] \quad (28)$$

for each pair of segments between consecutive objects  $i$  and  $i+1$ ,  $j$  and  $j+1$  along the chains (see Fig. 1). Notably these objects could be either beads or entanglements. When the sign of this volume changes from one numerical time step to another, the infinite lines corresponding to these segments have crossed. As shown in Fig. 3, the crossing point will result in an actual entanglement only when it belongs to both chain segments. The PB method employs a linear interpola-

tion formula in order to find the time instant at which  $V^{ij}$  becomes zero, as well as the corresponding segment end positions  $\mathbf{r}_0^i, \mathbf{r}_0^{i+1}, \mathbf{r}_0^j, \mathbf{r}_0^{j+1}$  at this time. When  $V^{ij}=0$ , the lines are coplanar, and the entanglement position  $\mathbf{r}^e$  satisfies the equation

$$\mathbf{r}^e = \mathbf{r}_0^i + \lambda_1(\mathbf{r}_0^{i+1} - \mathbf{r}_0^i) = \mathbf{r}_0^j + \lambda_2(\mathbf{r}_0^{j+1} - \mathbf{r}_0^j), \quad 0 < \lambda_1, \lambda_2 < 1. \quad (29)$$

Coplanarity implies that any two components of the vector equation (29) could be solved in terms of  $\lambda_1$  and  $\lambda_2$  (all possible combinations give identical values). Although in exact computations this is a correct statement, it is problematic in the context of numerical calculations. The linear  $V^{ij}$  interpolation does not guarantee that indeed the segment lines cross and are coplanar at the interpolated time at which we approximate  $V^{ij}=0$ . In this case, different combinations of the components of Eq. (29) can result in widely different  $\lambda_1, \lambda_2$  values. The situation is illustrated in Fig. 4.

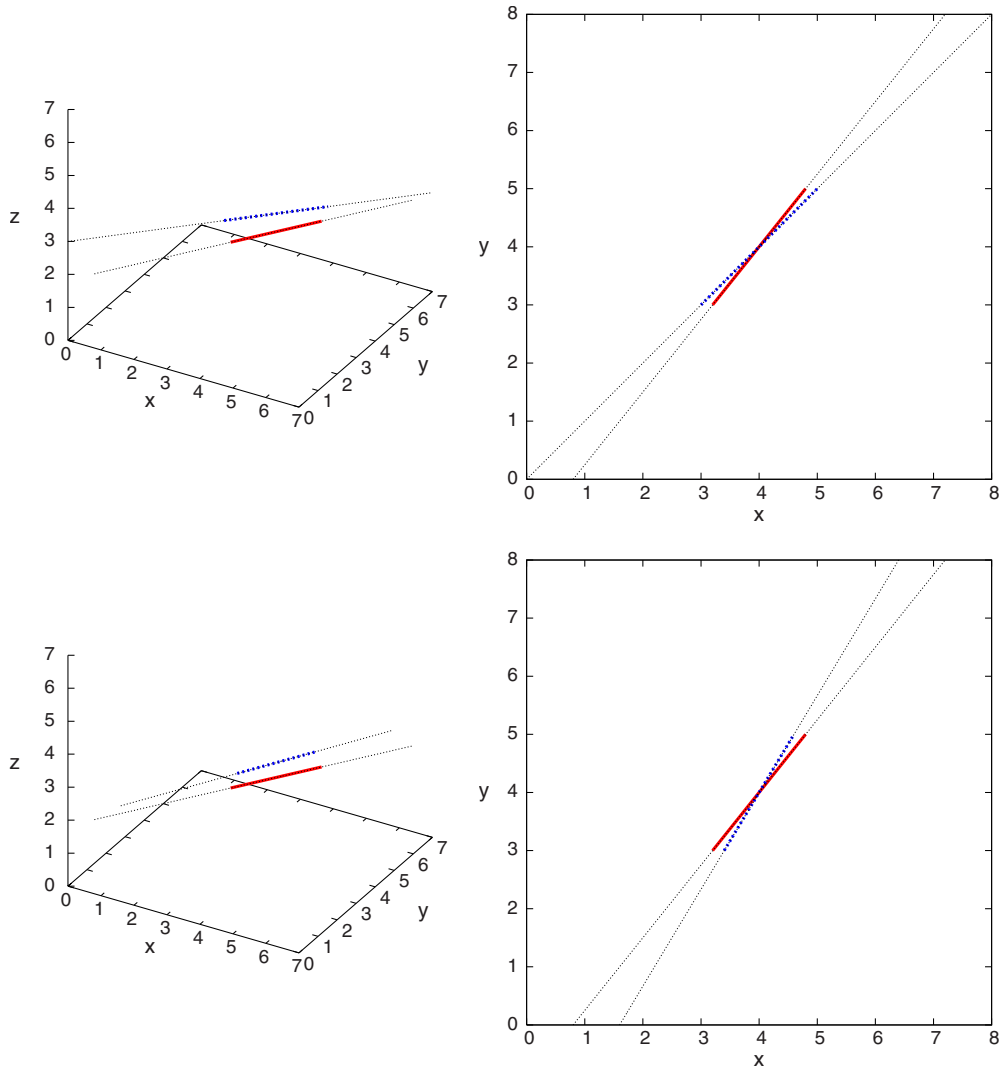


FIG. 4. (Color online) The top graphs show two neighboring chain segments (the left graphs are in three-dimensional space, while the right graphs show projections on the  $x$ - $y$  plane). During a numerical time step, the segments move to new positions (bottom graphs), and the sign of volume  $V^{ij}$  changes since their corresponding infinite lines cross far away from the segment positions.

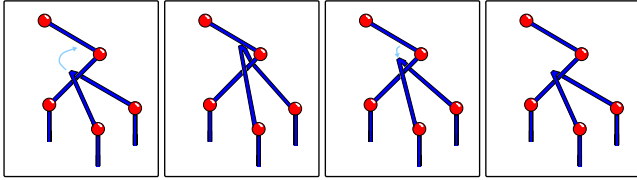


FIG. 5. (Color online) A case where the trial passing of an entanglement over a bead should result in the recovery of the original chain configuration.

The figure shows two neighboring chain segments in an initial configuration (top graphs) and their new positions (bottom graphs) after one numerical time step has elapsed. Since their corresponding infinite lines cross during their motion, the sign of volume  $V^{ij}$  changes. Following PB, a linear  $V^{ij}$  interpolation provides the time  $t_0$  when  $V^{ij}=0$ . However, due to the inaccuracy of the approximation, the interpolated segment positions are not actually in contact with one another at  $t_0$ . Then, it is easy to verify that the three possible component combinations (1,3), (1,2), (2,3) of Eq. (29) do not lead to equivalent conclusions. In the case shown, the (1,3), (2,3) choices correctly suggest that the segments have not passed through each other, but the choice (1,2) gives  $0 < \lambda_1, \lambda_2 < 1$ . Thus, with this combination, the entanglement criteria would be (falsely) satisfied, and an anomalous entanglement would be introduced into the calculation. The solution is, whenever  $V^{ij}$  changes sign, compute  $\lambda_1, \lambda_2$  with each of the combination of components of vector equation (29). Then conclude that an entanglement should be introduced only when the obtained  $\lambda$  values do not differ greatly between the methods, and their values all lie between zero and unity. This algorithm is particularly useful in disentanglement detection since without it spurious phantom chain events can occur, which destroy the integrity of a polymer knot.

(b) What happens when an entanglement approaches a bead? The analytical part of the mathematical model does not describe processes where an entanglement passes over a bead. Such nontrivial processes need to be performed at a computational level. As shown in Ref. [32], in some cases the movement of an entanglement over a bead (a so-called “overpass”) can result in a disentanglement (for example, when the bead is at the end of a chain), and hence the entanglement ought to be removed from the data structures. In all other cases, the Padding and Briels method passes the entanglement over the bead, and the entanglement remains in existence in its new position. This practice can result in a phantom chain process that falsely unknots the polymer. For example, in the chain configuration of Fig. 5, the passing of the entanglement over the bead should result in the elastic tension pulling the entanglement back to its original position. With the help of Figs. 6–8, we explain why this is not what happens in an actual computation. In particular, let us consider (Fig. 6) the entanglement between chain segments  $i-ip$  and  $j-jp$  as it approaches bead  $jp$ .

Passing the entanglement over this bead is computationally equivalent to the motion of segment  $j-jp$  to position  $jp-jpp$  (with objects  $i$  and  $ip$  remaining stationary) since, as far as the entanglement is concerned, the overpass is inter-

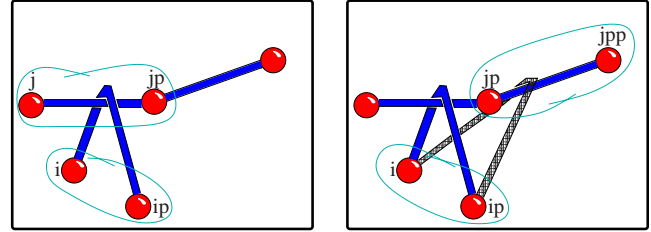


FIG. 6. (Color online) An entanglement between chain segments  $i-ip$  and  $j-jp$  approaches bead  $jp$ . As far as the entanglement is concerned, its passing over the bead is computationally equivalent to the movement of segment  $j-jp$  to a “new” position  $jp-jpp$ .

preted as a motion of the positions of objects  $j$  and  $jp$ . Extending this notion, it follows that overpasses correspond to motions of the infinite lines attached to the involved segments as shown in Fig. 7. When these infinite lines cross (as in Fig. 7, right), the sign of the postoverpass entanglement volume  $V^{ij}$  will differ from that of the preoverpass configuration. Indeed,  $V^{ij}$  changes sign in the case of Fig. 8, which is the computational counterpart of Fig. 5. Subsequently, as discussed previously, if such an overpass was allowed to take place, the algorithm would conclude that the entanglement ought to be removed, and the phantom chain effect becomes apparent by comparing the end results in Figs. 5 and 8.

Algorithmically, we can avoid such problems by computing the sign of the projected postoverpass  $V^{ij}$  volumes of entanglements that have approached beads. When the sign changes, no overpass should take place. It is better to allow the entanglement to remain in the neighborhood of the bead until, at a later time, a suitable configuration appears and a valid overpass is allowed.

(c) Padding and Briels indicated three cases where the passing of an entanglement over a bead results in a disentanglement. We found that two of them—i.e., disentanglement when the bead is at the chain end and when the overpass results in a forbidden entanglement of a chain segment with itself—are always valid and necessary. The third case involves a disentanglement when (in the preoverpass geometry) one of the four entanglement arms passes through the base of a tetrahedron formed by the objects at the ends of the other three arms [32]. Our calculations have indicated that this particular configuration arises in many cases where a disentanglement results in phantom chain effect and the knot topology is not preserved. In our computational model, when we detect such a geometric situation, we avoid passing the entanglement over the bead, and we wait until subsequent chain geometry allows either a valid overpass or a disentanglement to be performed.

### III. METHODS

On the numerical analysis side, we note that the Langevin equation (6), which is obtained in the Brownian limit of solution dynamics, retains information about bead momentum relaxation, i.e., it could be solved with time steps much smaller than the momentum relaxation time  $t_m = m_b / (6\pi\eta_s a)$  and provides information about bead velocity

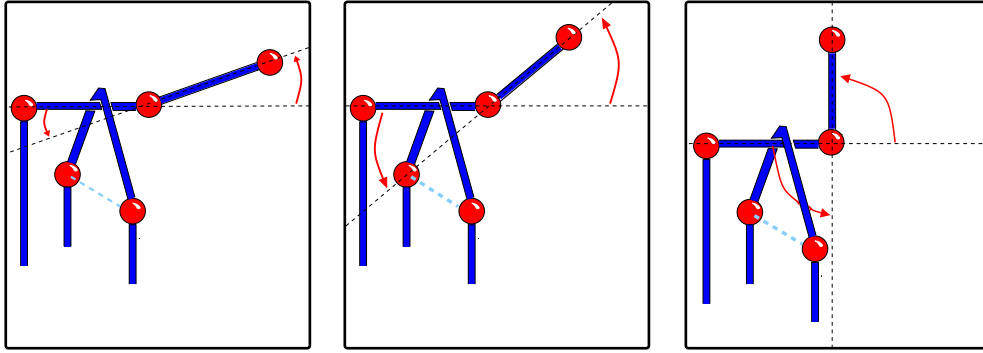


FIG. 7. (Color online) The entanglement volume  $V^{ij}$  changes sign after an overpass, when the infinite lines attached to the involved segments cross (right diagram).

correlations [34,47]. Such processes are not of interest to us, and we solve Eq. (6) in the diffusive limit resolving only position relaxation processes (which we assume to be well separated in time from the momentum relaxation processes). Working in this limit, we employ the first-order accurate scheme of Ermak and McCammon [58],

$$dr_i = \left[ u_j + \sum_{j=1}^{3N_b} \frac{\partial D_{ij}}{\partial r_j} + \sum_{j=1}^{3N_b} \frac{D_{ij}(eF_j + evF_j)}{k_B T} \right] dt + \sqrt{2} \sum_{j=1}^{3N_b} B_{ij} dW_j, \quad (30)$$

where  $\mathbf{D} = \mathbf{B} \cdot \mathbf{B}^T$  as required by the fluctuation-dissipation relation. Notably, the second term on the right-hand side of Eq. (30) becomes zero when the RPY diffusion tensor is employed. Moreover, in the diffusive limit of interest to us, we can also assume that the bead velocity distribution has enough time to equilibrate and becomes a Maxwellian. Applying this assumption to the formula for the polymer-induced stress, one obtains a simpler expression for the contribution of bead motion [36],

$$\boldsymbol{\sigma}^p = \nu \sum_{s=1}^{N_{s,c}} \left\langle \sum_{q=q^c(s)}^{q^c(s)+N_{q,s}^c(s)-1} \mathbf{Q}^q \cdot e\mathbf{F}^q \right\rangle - \nu \sum_{b=1}^{N_{b,c}} \sum_{s=1}^{N_{s,c}} B_{bs} \langle \mathbf{Q}^s \cdot ev\mathbf{F}^b \rangle - \nu N_{s,c} k_B T \mathbf{I}. \quad (31)$$

The importance of polymer-induced stresses in the flow is parametrized by the apparent Trouton ratio

$$\text{Tr}^a = \frac{\eta_E}{\eta_s}, \quad (32)$$

where  $\eta_E$  is the transient extensional viscosity

$$\eta_E = \frac{\sigma_{11} - \sigma_{33}}{\dot{\epsilon}}. \quad (33)$$

We solve the Ermak and McCammon stochastic differential equation with an explicit Euler scheme. The matrix  $\mathbf{B}$  is computed via the Cholesky decomposition of  $\mathbf{D}$ . The stochastic vector  $d\mathbf{W}$  is Gaussian with mean value zero and variance  $\delta t$  (where  $\delta t$  is the time step of the Euler scheme). In order to avoid very small numbers in the diffusion matrix, we scale our problem so that the diagonal elements of  $\mathbf{D}$  become equal to unity. The scaling units are  $l^* = b_K$ ,  $t^* = 6\pi\eta_s ab_K^2 / (k_B T)$ , and  $m^* = (6\pi\eta_s ab_K)^2 / (k_B T)$ , for length, time, and mass, respectively. The numerical time step  $\delta t$  needs to ensure the resolution of both chain relaxation and flow processes. The flow time scale is readily given by  $\tau_f = 1/\dot{\epsilon}$ , and the smallest chain relaxation scale is  $\tau_0$ . In addition, since our numerical method is only first order accurate in time, we avoid taking large time steps and choose an empirical factor  $f_r = 10^{-2}$  for independently restricting  $\delta t$ . In the end,  $\delta t = f_r \min(\tau_0, \tau_f)$ . Finally, we have employed the Polak-Ribiere variant of the Fletcher-Reeves version of the conjugate gradient algorithm [59] for the computation of en-

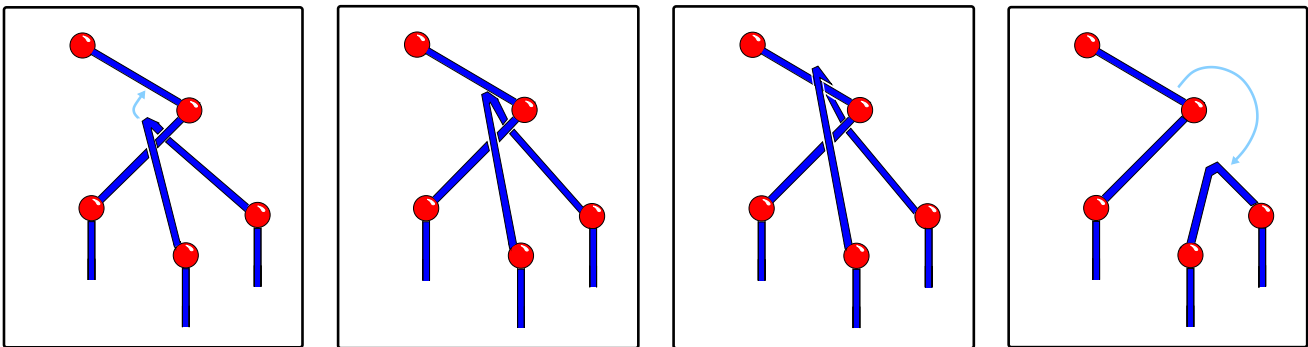


FIG. 8. (Color online) In this case, passing the entanglement over the bead (within the computational model) results in the removal of the entanglement and a phantom chain effect.

tanglement positions via the optimization of elastic energy  $e\Phi$ .

On the computational informatics side, we note that entanglement related data structures must be carefully chosen in order to accommodate the need for a dynamic number of entanglements and connectors, while effectively encoding information about which objects and in which order comprise the polymer chains in the system. We have found that the introduction of twin collocated entanglements at the crossing point of two chains (one for each chain that participates in the crossing) reduces the algorithmic complexity. During a computational time step, we first compute the new bead positions by solving the governing Langevin equation. With the new bead positions, we compute the diffusion matrix and bead-bead excluded volume interactions since these quantities do not depend on the positions of the entanglements. Next, we minimize the elastic energy and update the positions of the entanglements carried over from the previous time step. Employing the updated object and connector positions, as well as their stored positions at the previous time step, we compute possible connector crossings, adding new entanglements in the data structures. Subsequently, we do all possible remeshing of the entanglements along each chain by passing entanglements over beads or exchanging the positions of neighboring entanglements. When the passing of an entanglement over a bead results in a disentanglement, the latter is performed at this algorithmic stage. After remeshing, we detect possible dynamic disentanglements (i.e., those due to the motion of objects according to physics rather than computational remeshing), and, subsequently, we remove all discontinued entanglements from the data structures. In the end, having updated the coordinates of all objects and having determined the entanglements to be carried over to the next time step, we compute the spring elastic forces and increase the time.

#### IV. RESULTS

We define our fluid  $\mathcal{F}=\{\mathbf{u}(\mathbf{x},t),\mathbf{r}^c(\xi,t)\}$ ,  $c=1,\dots,N_c$  as an (infinite) set of values that are given at an initial time instant and subsequently evolve according to physical laws under constraints imposed by boundaries (Cauchy problem). Although the well posedness of the Cauchy problem in the case of simple FENE dumbbells has been discussed before [60–63], there are no similar results for the more complicated model employed here; thus, in order for the model to be empirically useful, we assume that its solutions exist. Moreover, in order to make contact between theory and experimentally measured mean values, we present results and conclusions by ensemble averaging over 40 system realizations. In order to compute the latter, we need to specify also input parameters that are included in the governing equations, but they do not belong to either the dependent or independent variables. We list these parameters here.

The working solution is an aqueous polyethylene oxide solution. The temperature is  $T=293.15$  K and the solvent viscosity is  $\eta_s=0.01$  g cm<sup>-1</sup> s<sup>-1</sup>. Notably, since we do not solve Eq. (1), the solvent mass density is not required. We do require, however, the polymer mass concentration  $c$  in the

computation of the number of polymers per unit solution volume  $\nu$ , which appears in the Kramers formula for the polymer contribution to the solution stress. Since all computations involve unbounded systems and a dilute solution, we can use any  $\nu\leq\nu^*$ , where  $\nu^*=N_A c^*/M$ , and  $c^*=M/(N_A R_c^3)$  is the overlap polymer mass concentration. We employ  $\nu^*$ , which is specified below. The polymer molecular mass is  $M=10^6$  Da, the experimentally determined Kuhn length is  $b_K=0.737\times 10^{-7}$  cm, and the number of Kuhn lengths per chain is  $N_{K,c}=11050$ . In order to extract the excluded volume  $v_{ev}$  from the experimental data, we define the concentrated solution volume fraction  $\phi_{**}\approx v_{ev}/b_K^3$ , i.e., the volume fraction for which the thermal blob length scale becomes equal to the correlation length scale; thus, excluded volume interactions are screened on all scales, and the chain obeys ideal chain statistics. Then, we rewrite Eq. (12) as

$$\tau_1^Z = \frac{\eta_s b_K^3}{k_B T} \phi_{**}^{6\nu-3} N_{K,c}^\nu. \quad (34)$$

In Ref. [37], we have measured the longest relaxation of our solution in the infinitely dilute regime and found  $\tau_1^e=0.0008$  s. By replacing  $\tau_1^Z$  with  $\tau_1^e$  in Eq. (34) and solving for  $\phi_{**}$ , we find  $\phi_{**}=0.3755$ . Finally, from the definition of  $\phi_{**}$ , we conclude that  $v_{ev}=0.15031\times 10^{-21}$  cm<sup>3</sup>.

All computations involve unbounded systems. The homogeneous strain rate is set to  $\dot{\epsilon}=2\times 10^3$  s<sup>-1</sup>; thus,  $De_1=1.6$ . Each chain is discretized with  $N_{b,c}=41$  beads. Consequently, the Deborah number based on the spring relaxation time is  $De_0=2.38\times 10^{-3}$  so, consistently with the hypotheses of our model, we can plausibly assume that the springs remain (approximately) in a thermodynamic steady state as the large scales of the polymer chain experience inertial stretching.

Next, we need to define the crucial empirical parameters  $\beta$  and  $h$ . We can fix two parameters by requiring that our model reproduces two independent experimental data. These are the longest relaxation time  $\tau_1^e=0.0008$  s and the experimental intrinsic viscosity  $[\eta]^e=571.9163$  cm<sup>3</sup> g<sup>-1</sup> [31]. In order to extract from  $[\eta]^e$  a directly computable quantity, we employ the scaling relation  $[\eta]\approx N_A R_c^3/M$  [39,40] and find  $R_c^e=0.983\times 10^{-5}$  cm. By following methods similar to those described in Ref. [37], after a trial and error procedure, when  $\beta=30$  and  $h=0.475$ , we obtain  $\tau_1=0.00072$  s and  $R_c=3.008\times 10^{-5}$  cm. Taking into account the scaling nature of the relation that we have employed in order to extract  $R_c$  from  $[\eta]$ , this is a reasonable agreement. Employing the experimental average end to end polymer extension  $R_c^e$ , we find  $c^*=3.0574\times 10^{-4}$  g cm<sup>-3</sup> and  $\nu^*=0.3088\times 10^{15}$  molecules/cm<sup>3</sup>. Finally, we mention that our code has been extensively tested both against established computational results and experimental rheological measurements, and these tests are documented in Ref. [37].

We have investigated the dynamics of figure-of-eight and granny knots. As Fig. 9 indicates, the figure-of-eight knot dynamics involves exclusively intramolecular topological constraints, while—since the granny knot is constructed from two polymer chains—its dynamics include intermolecular entanglements. For each knot, we perform two series of computations with identical initial conditions. The first is

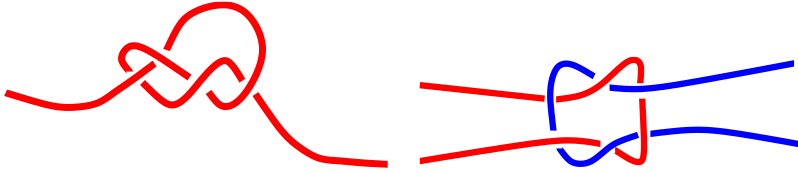


FIG. 9. (Color online) The figure-of-eight knot (left) is modeled with one polymer chain, while the granny knot (right) is modeled with two polymer chains.

performed with ECD and the second is performed with phantom chain dynamics (PCD). In this way, the effect of the knot becomes apparent since “knotted” polymer configurations do not have any dynamical significance in PCD. In all initial conditions, the knot is realized by a third of the chain segments. In each series, we first prepare an equilibrium configuration state by starting with a knot of length close to its equilibrium value and by evolving it for five Zimm longest relaxation times. After short transients, the polymer length starts fluctuating around its equilibrium value. Subsequently, we apply a uniaxial extensional flow with a rate of strain  $\dot{\epsilon}=2 \times 10^3 \text{ s}^{-1}$  and a corresponding Deborah number  $De_1=1.6$ .

#### A. Figure-of-eight knot

The major results are summarized in Fig. 10. Data from a corresponding PCD computation with the same initial conditions are also shown there (upper curves) for comparison.

Overall, the model predicts departures of ECD results from corresponding PCD data during the intermediate and final stages of the approach to steady state. The entangled chains stretch more slowly than the phantom chains, and their steady state corresponds to smaller polymer-length val-

ues (Fig. 10, top left). The polymer contribution to the stress (Fig. 10, bottom left) and Trouton ratio values (Fig. 10, bottom right) allow similar conclusions. Notably (Fig. 10, top right), the number of entanglements  $N_e$  presents a peak before the onset of polymer-length steady state. This peak is followed by  $N_e$  relaxation to a steady-state value close to 4.

In order to explain these data, we analyze the chain configurations that our model predicts (Fig. 11). The basic conclusion is that the model accurately describes the tightening of the figure-of-eight knot under the influence of the applied strain. Indeed, the initial knot configuration of Fig. 11(a) is first allowed to relax in a stationary solvent. As shown in Fig. 10 (top left), the (mean) chain length is constant during this period. Notably, in the PCD computations, all figure-of-eight knot topologies in the initial configurations are destroyed by the end of this phase. Only in very few cases (three out of 40) the chain remains knotted by becoming (after some phantom chain crossings) a trefoil knot. Despite this, and in contrast with the granny knot case, ECD and PCD predict identical equilibrium length values. As shown in Fig. 11(b), the ECD model preserves the integrity of the knot since it detects chain crossings and obstructs them by introducing entanglements (the three spheres in the image). In fact, we had to extend the Padding and Briels method in order to

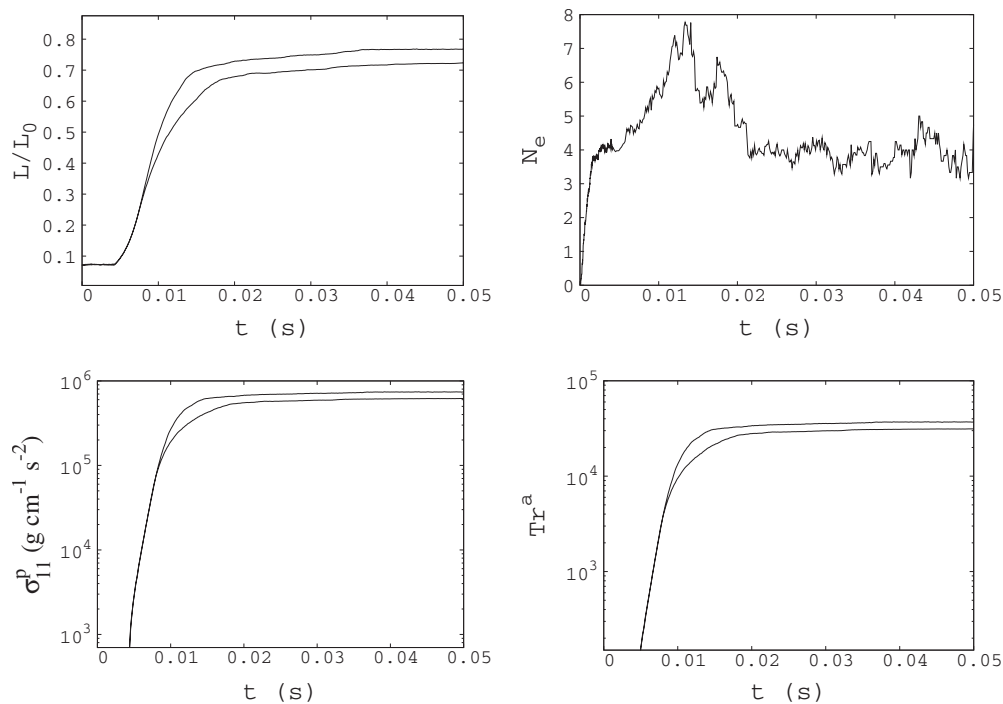


FIG. 10. Figure-of-eight knot results. The upper curves correspond to phantom chain dynamics and have been displayed for comparison with entangled chain dynamics results (lower curves). Top left: normalized chain length  $L/L_0$  versus time  $t$ . Top right: number of entanglements  $N_e$  versus time. Bottom left: polymer contribution to the stress along the extensional direction  $\sigma_{11}^p$  versus time. Bottom right: apparent Trouton ratio  $Tr^a$  versus time.

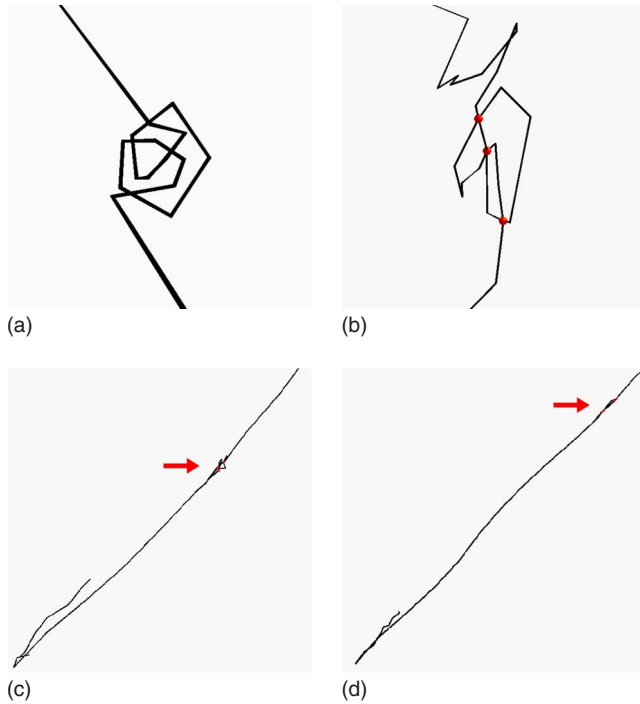


FIG. 11. (Color online) Figure-of-eight knot configurations demonstrating knot tightening. Time increases from the top-left graph toward the bottom-right graph as follows: (a)  $t_a=0$  s, (b)  $t_b=0.417 \times 10^{-2}$  s, (c)  $t_c=0.953 \times 10^{-2}$  s, and (d)  $t_d=1.550 \times 10^{-2}$  s. For clarity, images are drawn with different scales. All figures show only a part of the macromolecule. In this particular realization, the chain reaches a steady state at  $t_d \approx 3.3 \times 10^{-2}$  s, when the fold in images (c) and (d) straightens up. The spheres indicate entanglement positions. The arrows indicate the position of the knot.

capture these effects correctly. Under the influence of the extensional strain rate, the knot shrinks. As shown in Fig. 11(c), the knot, which initially comprised one third of the chain, becomes highly localized. At this time, it still has a discernible inner structure. The rest of the molecule is not affected by knot shrinking and unravels like an ordinary polymer via fold relaxation. The stretching of single linear

molecules in a variety of flows is a thoroughly studied process [37,64–67], but previous theoretical studies were performed with PCD and did not include self-entanglement effects. The deviation of ECD results from the corresponding PCD data is only partially due to the figure-of-eight knot topology; a significant contributing factor is the mere presence of self-entanglements between folded chain segments that obstruct the unraveling action of the applied flow. By the time of Fig. 11(d), the knot has collapsed to a very small region, which—in the scale of the fully stretched polymer—is pointlike and barely discernible. Notably, the knot cannot shrink to an ideal point in our numerical calculations. Its microstructure consists of small chain segments that are prevented from unraveling. This is the main reason that the knotted polymer steady-state length and polymer contribution to the stress are smaller than the corresponding PCD values. Another reason is the occurrence of rare perplexed chain configurations (Fig. 12) that unravel very slowly in time. In particular [Fig. 12(a)], in some rare cases, the polymer folds almost symmetrically with the knot at the base of the fold. Subsequently, the two parallel segments slide relatively to each other, a process that, if brought to completion, would eventually unknot the polymer. However, knot tightening prevents this from happening by terminating the sliding process, and self-entanglements cause the two arms of the fold to entwine [Fig. 12(c)], creating a perplexed polymer section [lower chain part of Fig. 12(b)] that unravels with great difficulty. Finally, the  $N_e$  dynamics are explained as follows: as the chain in general, and the knot in particular, collapses onto the stretching axis under the influence of the flow, the number of entanglements increases. There are two kinds of entanglements: (a) entanglements that preserve the integrity of the knot and persist in time and (b) entanglements between chain segments that obstruct each other's motion without forming any nontrivial topological structure. The peak in  $N_e$  corresponds to the approximate tightening of the knot and does not signify the onset of steady state since, as shown in Figs. 11(c) and 11(d), there might be residual folds in the system (carrying their own entanglements) that need to relax before steady state is achieved. As these folds straighten up, the number of entanglements falls. Finally, when the whole molecule is fully stretched, there exist only

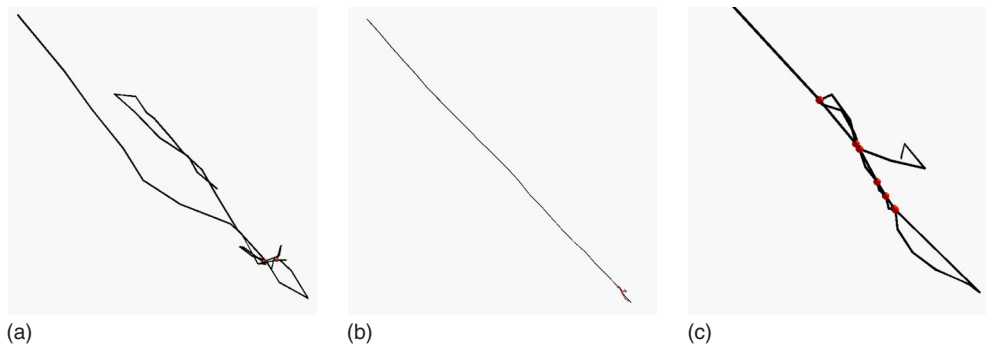


FIG. 12. (Color online) Figure-of-eight knot configurations demonstrating perplexed chain segments induced by knot tightening. Time increases from left to right graph as follows: (a)  $t_a=1.55 \times 10^{-2}$  s, (b)  $t_b=0.16810$  s, and (c)  $t_c=t_b$  (magnified detail of the lower end of the chain). For clarity, images are drawn with different scales. Figures (a) and (b) show the whole molecule. In the rare case depicted here, the tightening of the knot (lower part of chain in the left figure) prevents the arms of the fold shown in (a) to slide relative to each other. In this way, the fold arms become entwined slowing down the extension rate. The spheres indicate entanglement positions.

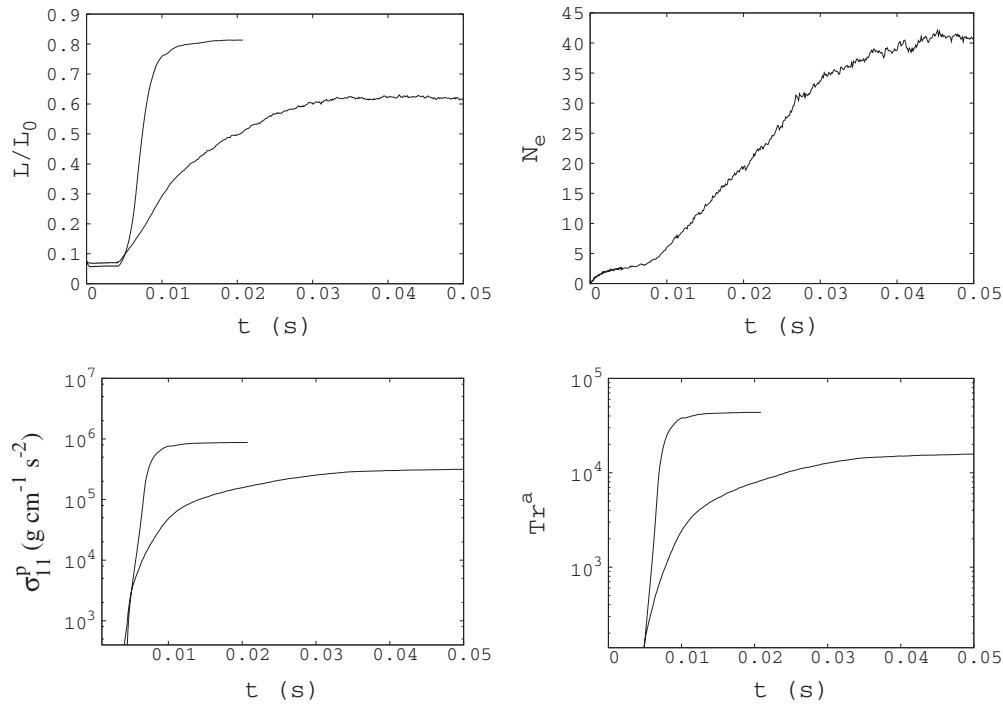


FIG. 13. Granny knot results. The upper curves correspond to phantom chain dynamics and have been displayed for comparison with entangled chain dynamics results (lower curves). Top left: normalized chain length  $L/L_0$  versus time  $t$ . Top right: number of entanglements  $N_e$  versus time. Bottom left: polymer contribution to the stress along the extensional direction  $\sigma_{11}^p$  versus time. Bottom right: apparent Trouton ratio  $\text{Tr}^a$  versus time.

the entanglements associated with the tightened figure-of-eight knot. Since this knot has four crossing points, one would expect on average four entanglements per molecule, which explains the steady-state value close to 4 in Fig. 10(b).

### B. Granny knot

The major results are summarized in Fig. 13. The results of a corresponding PCD computation with the same initial conditions are also shown there (upper curves) for comparison.

Overall, the model predicts (top left of Fig. 13) that the knotted polymers are stretched much slower than the phantom chains, and their steady-state length is significantly smaller than the corresponding value in the PCD computation (which is close to 0.8 of the maximum length). The polymer contribution to the stress (bottom left of Fig. 13) and Trouton ratio values (bottom right of Fig. 13) allow similar conclusions. Notably (top right of Fig. 13), knot stretching is accompanied by the growth of the number of entanglements  $N_e$ . Equally important, the number of entanglements and the polymer length reach steady state simultaneously.

In order to explain these data, we analyze the chain configurations that our model predicts (Fig. 14). The basic conclusion is that the model accurately describes the tightening of the granny knot under the influence of the applied strain. Indeed, the initial knot configuration of Fig. 14(a) is first allowed to relax in a stationary solvent. As shown in Fig. 13 (top left), following a short transient, the length relaxes to its equilibrium value. It is important to note that, in the PCD computations, all knot topologies are destroyed within this

initial equilibration period. This impacts directly on the length dynamics since the destruction of knot topology in the PCD case invigorates the polymer-length relaxation resulting in a smaller equilibrium length. As shown in Fig. 14(b), the ECD model preserves the integrity of the knot since it detects chain crossings and obstructs them by introducing entanglements (indicated as spheres in the image). These effects could only be captured by the present ECD model. Following the application of uniaxial extension, the knot starts shrinking as shown in graphs of Figs. 14(c) and 14(d). During this period, the number of entanglements grows since the dynamics favor (a) the collapse of the knot to a point [central area of Fig. 14(e)] and (b) the collapse of the chain arms not participating to the knot onto a highly straightened fold. Both processes create numerous contacts between polymer segments. However, the first process generates dynamically important entanglements that tighten the knot, forming eventually a chain link, while the second process simply generates points of contact (“friction”) between two otherwise parallel chain segments [discernible after magnification in Fig. 14(f)]. At later times, the number of these contact entanglements achieves a dynamic equilibrium under the influence of thermal chain contour fluctuations [Fig. 14(f)]. Now, in the PCD case, following the destruction of the knot, the two chains evolve practically independently of one another. Flow drag causes a sequence of chain configurations that result in the full extension of both chains. In the ECD case, the knot is responsible for the persistence of entanglements that obstruct flow-induced stretching-facilitating polymer motions. Consequently, the knotted chains stretch with a much slower rate. What is the major dynamical effect of knot

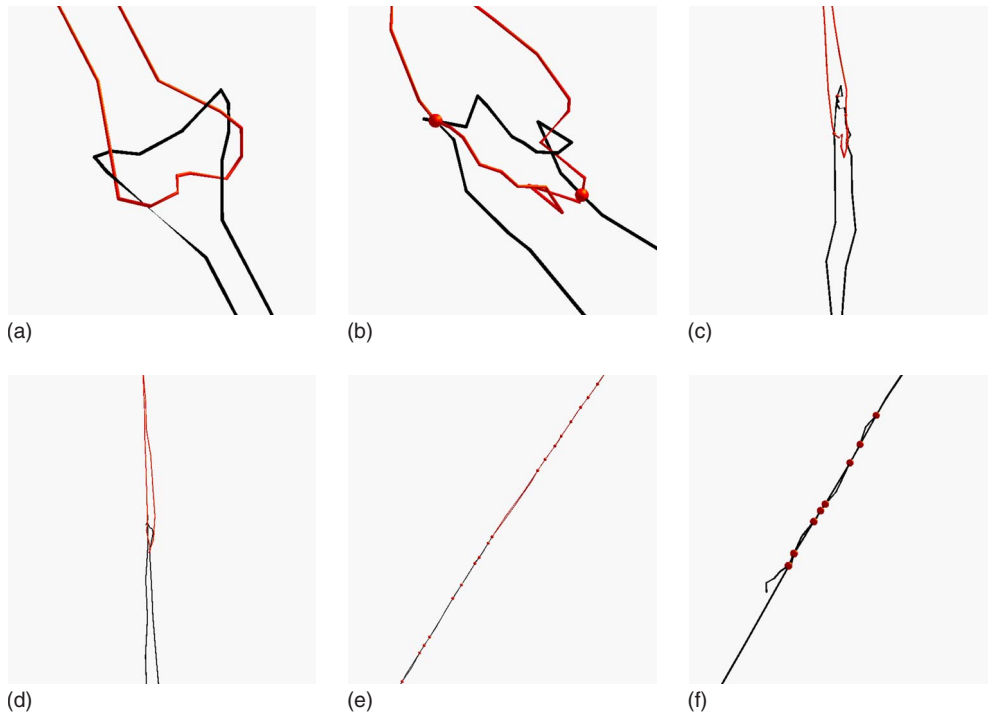


FIG. 14. (Color online) Granny knot configurations. Time increases from the top-left graph toward the bottom-right graph as follows: (a)  $t_a=0$  s, (b)  $t_b=0.417 \times 10^{-2}$  s, (c)  $t_c=0.953 \times 10^{-2}$  s, (d)  $t_d=2.026 \times 10^{-2}$  s, (e)  $t_e=4.292 \times 10^{-2}$  s, and (f)  $t_f=t_e$  (magnified detail of the lower chain). The spheres indicate entanglement positions.

tightening? This becomes clear by observing that, once the polymer has collapsed onto a fold of two parallel segments, the fold can only relax by having its arms sliding relative to each other. This process has been computed from first principles in Ref. [37] (Fig. 10 there). Now, as long as the knot has not fully tightened, the sliding process progresses. If allowed to reach completion, this process would eventually untie the knot, releasing the two chains and allowing them to stretch fully. In other words, the steady-state length and stress levels would be similar to the PCD case. However, the full tightening of the knot at  $t \approx 0.037$  s prevents this. Indeed, following this event, the folds cannot be eliminated via sliding. The two arms of each fold necessarily overlap with each other, and hydrodynamic interactions shield the beads from the imposed flow (in a similar fashion with the Zimm theory). Consequently, the total drag experienced by the chains is reduced, and the latter do not need to stretch as much as in the PCD case in order to balance the (reduced) flow-induced drag. In the end, the tightening of the knot is responsible for the smaller (in comparison with the unknotted case) elastic stress levels that a granny knot can support in an extensional flow.

## V. CONCLUSION

We formulated a coarse-grained entangled chain dynamics model of polymers in solution. The model splits excluded volume interaction effects in two categories: (a) bead-bead excluded volume interactions that are modeled physically via pairwise potential forces and disfavor bead overlap and (b) spring-spring contact interactions that explicitly enforce

chain uncrossability and are modeled geometrically by extending the model of Padding and Briels [32]. Our model captures the persistence of knot topologies of macromolecules in solution. We applied it to the dynamics of figure-of-eight and granny knot polymers in strong uniaxial extensional flows ( $De=1.6$ ). Our main conclusions are that knots slow down the stretching of individual polymers by obstructing via entanglements the “natural,” unraveling, and flow-induced chain motions. Moreover, the steady-state length values are smaller in knots than in topological trivial chains. These effects are much stronger in the granny knot case. This is because, in the latter case, knot tightening prevents full relaxation of folded chain configurations producing entwined chain segments that shield (via hydrodynamic interactions as shown by Zimm) the beads from the effects of flow drag. The evolution of the number of entanglements depends on the particular knot type. In the granny knot case, knot tightening leads to persistent entanglements between kinematically collapsed chain segments; thus, there are numerous non-knot-associated entanglements during steady state. On the other hand, in the figure-of-eight knot case, knot tightening is—most of the time—a local process without a great influence on polymer dynamics; and, at steady state, the number of entanglements is solely associated with the collapsed knot structure, i.e., it is approximately equal to the crossing number of the knot.

The present theoretical results can be checked by feasible experiments. Indeed, Perkins *et al.* [67] already experimented with the dynamics of single unknotted macromolecules in extensional flow. On the other hand, Bao *et al.* [26] used optical tweezers and tied individual polymers in knots. Therefore, a combination of these existing techniques can

provide experimental tests of some of the model's predictions.

From the theoretical point of view, it is important to develop methods for the mathematical analysis of the proposed model in bounded or periodic domains. This will allow a direct comparison of the model's predictions with data from rheological experiments involving dense solutions. In this context, we note that, in order to compute high De number flows, we need an implicit scheme. The latter cannot be the semi-implicit scheme of Somasi and co-workers [41,37,68] since it presupposes that the lengths of the spring connector vectors are also the lengths of the springs, which is not valid in our model. Instead, we could use more general implicit schemes like, for example, Newton's method [69].

Finally, the model could be employed in order to examine the assumptions of more macroscopic tube theoretic models of entangled solutions and in close interaction with these theories to suggest ways for their further development. In this context, it is important to note that the "elementary" entanglements computed here are not identical to the "effec-

tive" entanglements of tube theory and other more phenomenological approaches. The latter represent collective topological chain restrictions due to many neighboring chains and encode statistical dynamical effects of the presently modeled elementary entanglements. Thus, any connections between CGMD and tube theoretic approaches ought to be based on procedures that, by performing appropriate processing of microscopic dynamics data, allow valid inferences about more macroscopic effective dynamics. Such a procedure, for example, is the "primitive path" analysis of Everaers and co-workers [70,71], as well as other analogous approaches [72–75].

#### ACKNOWLEDGMENTS

This work was supported by the Joint Science and Technology Office, Defense Threat Reduction Agency (JSTO/DTRA) and the National Ground Intelligence Center (NGIC).

- 
- [1] S. F. Edwards, Proc. Phys. Soc. **91**, 513 (1967).  
 [2] M. Doi and S. F. Edwards, *The Theory of Polymer Dynamics* (Oxford University Press, Oxford, 1986).  
 [3] G. Marrucci, Science **301**, 1681 (2003).  
 [4] P.-G. de Gennes, Macromolecules **17**, 703 (1984).  
 [5] P.-G. de Gennes, J. Chem. Phys. **55**, 572 (1971).  
 [6] G. A. Arteca, Theor. Chem. Acc. **118**, 549 (2007).  
 [7] D. W. Sumners and S. G. Whittington, J. Phys. A **21**, 1689 (1988).  
 [8] E. J. J. van Rensburg and S. G. Whittington, J. Phys. A **23**, 3573 (1990).  
 [9] E. J. J. van Rensburg, D. A. W. Sumners, E. Wasserman, and S. G. Whittington, J. Phys. A **25**, 6557 (1992).  
 [10] P. Virnau, Y. Kantor, and M. Kardar, J. Am. Chem. Soc. **127**, 15102 (2005).  
 [11] M. Kardar, Eur. Phys. J. B **64**, 519 (2008).  
 [12] W. Thomson, Philos. Mag. **34**, 15 (1867).  
 [13] L. Faddeev and A. J. Niemi, Nature (London) **387**, 58 (1997).  
 [14] T. Itano and S. C. Generalis, Phys. Rev. Lett. **102**, 114501 (2009).  
 [15] *Geometric and Topological Methods for Quantum Field Theory*, edited by H. Ocampo, S. Paycha, and A. Vargas (Springer, Berlin, 2005).  
 [16] D. Kivotides and A. Leonard, EPL **63**, 354 (2003).  
 [17] C. F. Barenghi, R. L. Rica, and D. C. Samuels, Physica D **157**, 197 (2001).  
 [18] A. F. Horn and E. W. Merrill, Nature (London) **312**, 140 (1984).  
 [19] D. W. Sumners, Not. Am. Math. Soc. **42**, 528 (1995).  
 [20] E. Ercolini, F. Valle, J. Adamcik, G. Witz, R. Metzler, P. De Los Rios, J. Roca, and G. Dietler, Phys. Rev. Lett. **98**, 058102 (2007).  
 [21] W. R. Taylor, Nature (London) **406**, 916 (2000).  
 [22] S. R. Quake, Phys. Rev. Lett. **73**, 3317 (1994).  
 [23] P.-Y. Lai, Phys. Rev. E **66**, 021805 (2002).  
 [24] E.-G. Kim and M. L. Klein, Macromolecules **37**, 1674 (2004).  
 [25] A. M. Saitta and M. L. Klein, J. Chem. Phys. **116**, 5333 (2002).  
 [26] X. R. Bao, H. J. Lee, and S. R. Quake, Phys. Rev. Lett. **91**, 265506 (2003).  
 [27] A. Vologodskii, Biophys. J. **90**, 1594 (2006).  
 [28] O. Farago, Y. Kantor, and M. Kardar, EPL **60**, 53 (2002).  
 [29] A. Y. Grosberg and Y. Rabin, Phys. Rev. Lett. **99**, 217801 (2007).  
 [30] Y.-J. Sheng, P.-Y. Lai, and H.-K. Tsao, Phys. Rev. E **61**, 2895 (2000).  
 [31] A. M. Saitta, P. D. Soper, E. Wasserman, and M. L. Klein, Nature **399**, 46 (1999).  
 [32] J. T. Padding and W. J. Briels, J. Chem. Phys. **115**, 2846 (2001).  
 [33] S. Kumar and R. G. Larson, J. Chem. Phys. **114**, 6937 (2001).  
 [34] I. Snook, *The Langevin and Generalized Langevin Approach to the Dynamics of Atomic, Polymeric and Colloidal Systems* (Elsevier Science, Amsterdam, 2007).  
 [35] G. H. Fredrickson, *The Equilibrium Theory of Inhomogeneous Polymers* (Oxford University Press, Oxford, 2006).  
 [36] R. B. Bird, C. F. Curtiss, R. C. Armstrong, and O. Hassanger, *Dynamics of Polymeric Liquids* (Wiley-Interscience, New York, 1989).  
 [37] D. Kivotides, V. V. Mitkin, and T. G. Theofanous, J. Non-Newtonian Fluid Mech. **161**, 69 (2009).  
 [38] V. Tirtaatmadja, G. H. McKinley, and J. J. Cooper-White, Phys. Fluids **18**, 043101 (2006).  
 [39] M. Rubinstein and R. H. Colby, *Polymer Physics* (Oxford University Press, Oxford, 2003).  
 [40] T. Kawakatsu, *Statistical Physics of Polymers* (Springer, Berlin, 2004).  
 [41] C. Hsieh, L. Li, and R. G. Larson, J. Non-Newtonian Fluid Mech. **113**, 147 (2003).  
 [42] R. M. Jendrejack, E. T. Dimalanta, D. C. Schwartz, M. D.

- Graham, and J. J. de Pablo, Phys. Rev. Lett. **91**, 038102 (2003).
- [43] S. P. Holleran and R. G. Larson, Rheol. Acta **47**, 3 (2008).
- [44] A. Blanchard, R. S. Graham, M. Heinrich, W. Pyckhout-Hintzen, D. Richter, A. E. Likhtman, T. C. B. McLeish, D. J. Read, E. Straube, and J. Kohlbrecher, Phys. Rev. Lett. **95**, 166001 (2005).
- [45] A. E. Likhtman, S. T. Milner, and T. C. B. McLeish, Phys. Rev. Lett. **85**, 4550 (2000).
- [46] D. W. Mead, R. G. Larson, and M. Doi, Macromolecules **31**, 7895 (1998).
- [47] A. J. Banchio and J. F. Brady, J. Chem. Phys. **118**, 10323 (2003).
- [48] R. G. Larson, *The Structure and Rheology of Complex Fluids* (Oxford University Press, Oxford, 1999).
- [49] A.-K. Tornberg and M. J. Shelley, J. Comput. Phys. **196**, 8 (2004).
- [50] J. M. Stockie and S. I. Green, J. Comput. Phys. **147**, 147 (1998).
- [51] C.-C. Hsieh and R. G. Larson, J. Rheol. **48**, 995 (2004).
- [52] R. Prabhakar, J. R. Prakash, and T. Sridhar, J. Rheol. **48**, 1251 (2004).
- [53] M. Kröger, A. Alba-Pérez, M. Laso, and H. C. Öttinger, J. Chem. Phys. **113**, 4767 (2000).
- [54] S. Kim and S. J. Karrila, *Microhydrodynamics* (Dover, Mineola, NY, 2005).
- [55] C. Pozrikidis, *Boundary Integral and Singularity Methods for Linearized Viscous Flow* (Cambridge University Press, Cambridge, England, 1992).
- [56] J. Rotne and S. Prager, J. Chem. Phys. **50**, 4831 (1969).
- [57] J. R. Goldman and L. H. Kauffman, Adv. Appl. Math. **18**, 300 (1997).
- [58] D. L. Ermak and J. A. McCammon, J. Chem. Phys. **69**, 1352 (1978).
- [59] W. H. Press, B. P. Flannery, S. A. Teukolsky, and W. T. Vetterling, *Numerical Recipes* (Cambridge University Press, Cambridge, England, 1992).
- [60] N. Masmoudi, Commun. Pure Appl. Math. **61**, 1685 (2008).
- [61] H. Zhang and P. Zhang, Arch. Ration. Mech. Anal. **181**, 373 (2006).
- [62] P. Constantin, C. Fefferman, E. Titi, and A. Zarnesku, Commun. Math. Phys. **270**, 789 (2007).
- [63] E. Weinan, T. J. Li, and P. W. Zhang, Commun. Math. Phys. **248**, 409 (2004).
- [64] R. G. Larson, H. Hu, D. E. Smith, and S. Chu, J. Rheol. **43**, 267 (1999).
- [65] J. S. Hur, E. S. G. Shaqfeh, and R. G. Larson, J. Rheol. **44**, 713 (2000).
- [66] Y.-L. Chen, M. D. Graham, J. J. de Pablo, G. C. Randall, M. Gupta, P. S. Doyle, Phys. Rev. E **70**, 060901(R) (2004).
- [67] T. T. Perkins, D. E. Smith, and S. Chu, Science **276**, 2016 (1997).
- [68] M. Somasi, B. Khomami, N. J. Woo, J. S. Hur, and E. S. G. Shaqfeh, J. Non-Newtonian Fluid Mech. **108**, 227 (2002).
- [69] R. M. Jendrejack, M. D. Graham, and J. J. de Pablo, J. Chem. Phys. **113**, 2894 (2000).
- [70] R. Everaers, S. K. Sukumaran, G. S. Grest, C. Svaneborg, A. Sivasubramanian, and K. Kremer, Science **303**, 823 (2004).
- [71] V. A. Harmandaris and K. Kremer, Macromolecules **42**, 791 (2009).
- [72] C. Tzoumanekas and D. N. Theodorou, Macromolecules **39**, 4592 (2006).
- [73] Q. Zhou and R. G. Larson, Macromolecules **38**, 5761 (2005).
- [74] K. Foteinopoulou, N. C. Karayiannis, and V. G. Mavrantzas, Macromolecules **39**, 4207 (2006).
- [75] S. Shanbhag and M. Kröger, Macromolecules **40**, 2897 (2007).